

Identification of Stochastic Manufacturing Defects Within Additively Manufactured Acoustic Liners

Joseph Windows¹, Alden Packer¹, Eric Nelson², Jeffrey Chowaniec, Jr.², Jeffrey Mendoza³,
C. Aaron Reimann³, Julian Winkler³, Kenji Homma³, and Nicholas Meisel^{*4}

* Corresponding Author: nam20@psu.edu

¹ Department of Mechanical Engineering, The Pennsylvania State University, University Park,
PA 16802

² Altair Engineering, Altair, Troy, MI 48083

³ RTX Technology Research Center, RTX, East Hartford, CT 06108

⁴ School of Engineering Design and Innovation, The Pennsylvania State University, University
Park, PA 16802

Abstract

The exploration of novel acoustic engine liner designs using 3D internal lattices has become a growing topic of interest within the field of additive manufacturing (AM) and the aeroacoustics community. However, the comparison between the acoustic liner response of computational simulation using the design intent and experimental testing of as-built structure can show significant deviation. While the deviation in performance will be explored in a future publication, this work analyses possible causes of the deviation. A potential cause is the inclusion of stochastic manufacturing defects within the part. This paper establishes methods for systematically identifying and quantifying defects in the printing of novel acoustic liners. This approach intends to offer up significant insight into the build quality of the printed lattice structures without the cost and time investment typically required of computed tomography (CT) scanning. The core of the liner design analyzed in this paper is made up of a triply periodic minimal surface (TPMS) Schwarz P lattice. Error distributions of several design variables are found by taking manual measurements of printed liners. Additionally, liners are scored using an automated screening method to detect significantly flawed prints. The potential for error distributions to be used in stochastic simulation studies could help predict what effect manufacturing defects have on the behavior of structures that leverage TPMS lattices with small features such as acoustic liners.

1. Introduction

Within the aviation industry there are numerous efforts to increase the efficiency of aircraft while also maintaining safe flight conditions. Unfortunately, the noise caused by aircraft engines can have burdensome or even harmful effects on the people and environment surrounding aircraft or airports [1]. One of the main countermeasures for reducing the auditory footprint of aircraft engines is the integration of acoustic liners inside the engine. The acoustic liners are typically located along the engine's nacelle inner boundary and absorb a significant amount of noise [2,3]. Although acoustic liners are already commonly used, there is still ongoing research to try to improve the absorptive capabilities of acoustic liners while reducing their overall mass and footprint. This is due to the fact that companies are trying to improve propulsive efficiency by increasing the engine's bypass ratio, which leads to the need for larger diameter fans. As fan size increases, the frequencies that the acoustic liners need to target become lower, leading to the need to increase the depth of traditional liners and taking up additional space within the engine [3,4].

There are two main types of acoustic liners currently being used in industry, both of which consist of a honeycomb lattice core enclosed by a rigid back plate and a perforated face sheet [5]. The first type, with only one perforated sheet and one layer of honeycomb lattice, is called a single-degree-of-freedom (SDOF) liner. The second type is called a double-degree-of-freedom (DDOF) liner. The difference between SDOF and DDOF liners is that DDOF liners include an additional perforated sheet called a septum that splits the honeycomb lattice into two layers. This can allow for more broadband frequency absorption, but cannot lower the first resonance frequency [3,4].

Since traditional liners take up additional space to capture lower frequencies, there has been a significant amount of research studying alternative types of liners. One promising approach leverages a triply periodic minimal surface (TPMS) lattice instead of a traditional honeycomb lattice. A TPMS is a mathematical surface that is made up of repeating unit cells in three dimensions and has zero mean curvature [6]. Such surfaces are defined by level-set equations using X, Y, and Z spatial cartesian coordinates, the number of cells in each direction, the total length of the surface in each direction, and a level-set constant (isovalue) controlling the volume fraction of the resulting lattice [7]. Thickening of the nominal isosurface created by level-set equations leads to a tangible TPMS lattice that can be used for mechanical, thermal, or acoustic purposes, though the latter is significantly less prevalent in research and practice [8–10]. The acoustic properties of these lattices are highly customizable and tunable without the necessity of changing the overall depth, giving them an advantage over the standard SDOF or DDOF honeycomb liners [10].

While the acoustic properties of TPMS lattices are promising, they tend to be difficult to accurately manufacture using traditional manufacturing methods due to their complex curved geometry [11]. The emergence and growth of additive manufacturing (AM) has greatly improved the ability to manufacture TPMS lattices of high quality, but as with any manufacturing process, there is still a degree of error in the final part [12]. The differences between as-designed and as-manufactured lattice structures can lead to significant deviations from the predicted acoustic performance of manufactured acoustic liners [13]. To successfully identify an optimal design for a TPMS-based acoustic liner, the ability to accurately predict the as-manufactured properties is of high importance. To do this, there must be a way to quickly and efficiently capture and quantify the defects and stochastic variability in the manufactured liners. This paper presents two different methods of systematically capturing such manufacturing defects in the printed cores of TPMS-based acoustic liner geometries, with the aim of being quicker and less expensive than traditional means of geometry capture and inspection (e.g., computed tomography (CT) scanning). This paper does not attempt to define an acceptable value for each defect based on the acoustic requirements (and other) of the structure. That is the focus of future studies.

2. Background

To fully recognize the need for a rapid and cost-efficient method of defect detection in TPMS acoustic liners, it is important to first understand (1) the types of defects that can arise in lattice structures and (2) what detection methods are currently used for identifying lattice defects. By harnessing the strengths and weaknesses of current inspection processes, new inspection methods can be established to increase efficiency while still providing ample feedback on the print quality without the need for the infrastructure typically required for CT scanning.

2.1. Types of Common Defects in Lattice Structures

While AM has become the method of choice for manufacturing complex 3D lattices, AM processes still introduce manufacturing flaws or inconsistencies into final products. Lattice-based imperfections can typically be divided into three categories: (1) microstructural defects [14]; (2) geometric defects [15]; and (3) post-processing defects [16,17]. Microstructural defects often include unwanted material porosity or surface roughness and are very dependent on the manufacturing process [18]. Differences in material porosity is most commonly seen as a concern in metal-based printing processes due to large thermal gradients created during the melting and solidification of the metal powder, which can lead to adverse effects on the mechanical properties of a lattice [19,20]. Surface roughness in lattices is also highly dependent on the printing process and can lead to stress concentrations at the surface of lattice struts [21]. Surface roughness can also impact the aerodynamic and acoustic performance of the liners of specific interest in this paper [22]. A study conducted by Kennedy et al. found that, despite similar geometric accuracy, a lattice manufactured using direct light processing (DLP) had a higher acoustic absorption coefficient than a lattice printed using stereolithography (SLA) due to a higher surface roughness [23].

Significant errors can also arise in the geometry of a printed lattice structure which can have significant impacts on the mechanical properties. For strut based lattices, geometric defects can include variable strut thickness, accumulation of excess material around strut joints, waviness in the struts, or even gaps in the lattice where a strut failed to print [24,25]. For TPMS lattices, geometric defects can include variation in pore sizes and wall thickness leading to lattice volume fractions that do not match the design variables [7,26,27]. These variations can directly affect the performance of the manufactured lattice. For example, Zhang et al. found in a comparison between simulated and experimental compression tests of a Schwarz-P lattice that the printed lattice exhibited a Young's modulus that was as much as 75% lower than the simulated results due to imperfect print geometry [28]. Additionally, Li et al. found that geometric deviations in an acoustic lattice test specimen printed using DLP led to a higher and slightly shifted acoustic absorption coefficient curve when compared to numerically calculated results [13].

The last type of lattice structure defects are flaws related to post-processing requirements which often affect functionality. While each type of AM technology has its own post-processing procedures, vat photopolymerization typically involves cleaning excess resin from the printed part and curing the cleaned part [29]. For complex lattices with small winding channels, such as TPMS lattices, resin can get trapped inside the part during the wash process leading to blockages within the final lattice [30]. Depending on the intensity of the wash method, lattices could also form cracks during the wash process [31]. Additionally, the curing process can cause shrinkage, and thus residual stresses in the part could cause fractures [32]. This can also lead to cracking or chipping of a delicate lattice during mechanical processes such as support removal [33].

2.2. Current Inspection Methods for AM Lattice Structures

Defect detection methods play a crucial role in determining the quality of a print, but there is a range of modern techniques, tools, and methods, all with different strengths and weaknesses. Currently, the most popular technology for defect detection in lattice structures is X-ray computed tomography (XCT) which can be used to create a computer model of the as-printed part to compare with the CAD modeled part [34,35]. Due to the extremely fine voxel resolution (typically 10-100 μm) that XCT is capable of, it is often a preferred option for not only defect detection, but also

dimensional evaluation, density measurements, and surface roughness analysis [36]. While the use of XCT in AM has proven helpful, it can impose significant cost, time, and resource constraints that make it intractable for certain applications [37]. Additionally, XCT tends to yield very large data volumes, which can be difficult to work with, and requires a sound understanding of the system's capabilities [38].

Although XCT may be considered the superior form of part inspection in many cases, microscopy is also a commonly used approach for dimensional analysis of lattice structures. There are two common forms of microscopy used to examine lattice structures, which are optical microscopy (OM), which uses light to magnify a desired surface, and scanning electron microscopy (SEM), which uses electron emissions to magnify the surface [39]. While microscopy is often used to inspect microstructures, it can also be used to inspect the unit cells of lattice structures. For example, Cansizoglu et al. used optical microscopy to compare the thickness of lattice struts at various build angles [40]. Additionally, both OM and SEM were used by Gabrieli et al. to examine the wall thickness and pore size of TPMS lattices printed with various design variables [41]. SEM can also be used to analyze the surface roughness of TPMS lattices which can have an impact on both structural and acoustic properties [42]. While microscopy is less expensive and faster than XCT, it still requires significant time and resources. Additionally, microscopy can require surface preparation of the specimen, which may be undesirable since it could change the topology of the as-manufactured surface [43].

While both XCT and microscopy techniques for part inspection have been leveraged in the past, there are also efforts to establish new part inspection methods specifically for AM lattice structures. For a strut-based lattice, Wilbig et al. found that mass and volume methods can distinguish between lattices with and without defects if the defects cause changes in mass and volume by 20% or more [44]. Another study by Obatan et al. showed that the use of resonant acoustic methods (RAM), along with machine learning, was able to identify and classify missing strut defects in a strut-based lattice with 80.95% accuracy and good reproducibility [45]. Additional work has been done to reduce the time commitment of traditional inspection methods like XCT. To reduce the time and resources needed for post-processing the XCT scans of a strut-based lattice, Zhang et al. incorporated artificial intelligence (AI) to automatically review the sliced images of the scan and detect structural defects [46]. While these novel methods aim to yield valuable insight into structural defects in strut-based lattices, very little literature has been established on finding a method that yields information about the stochastic manufacturing variation of printed lattices. Additionally, most studies related to defect detection methods primarily focus on strut-based lattices. As such, the remainder of this paper will be focused on two low-cost, systematic methods for capturing stochastic manufacturing variation and defects in additively manufactured TPMS lattice structures designed for acoustic absorption purposes.

3. Defect and Stochastic Error Detection Methods

This section explores two potential methods for rapid cost-efficient analysis of defects and stochastic error in manufactured acoustic liners without the need for extensive resources involved in current inspection methods like XCT. Both methods are designed to screen for surface level defects and dimensional accuracy, but are not intended for full 3D part inspection. The first uses a combination of manual measurements and image processing tools to find the average

manufactured deviation in the printed liners. From these measurements, approximate distributions can be found for the printed variation of the liner design variables. The second method uses image processing and machine learning to determine print consistency and identify major defects within the printed liners. From this method, the total number of defects is output, which can be used to judge the overall print quality for screening. Since these methods were developed considering a specific liner design framework, this section starts with an overview of the design process before moving to defect identification.

3.1 Overview of Liner Design and Manufacturing

To allow for the removal of excess resin in the lattice core of the acoustic liner used in this paper, the liner is printed as two pieces and assembled after printing. The two parts are referred to as the liner casing and the liner core as shown in Figure 1. The liner casing acts as the housing for the liner core to slot into. The liner core consists of a TPMS Schwarz-P lattice structure connected to a perforated face sheet. A Schwarz-P lattice is chosen because it was found to have promising acoustic performance during preliminary tests. The face sheet is designed with an arbitrary pattern and allows acoustic waves to pass into the liner core [47]. Since the core is significantly more complex, thus more prone to possible defects and more challenging to evaluate, it is the focus of the analysis methods discussed in this work.

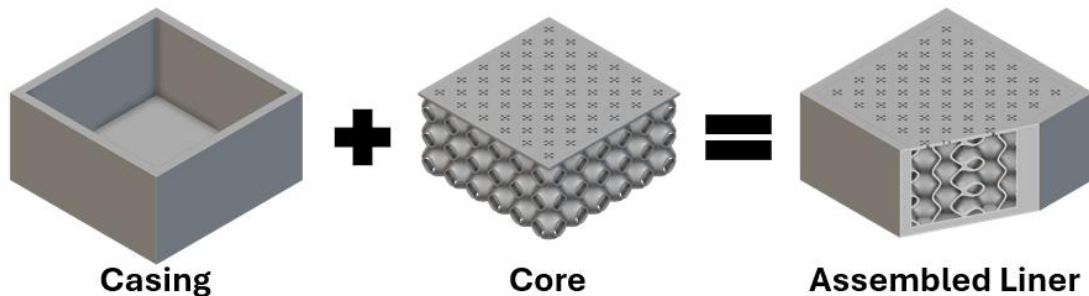


Figure 1. Acoustic sample design.

The liner core is modeled using nTop for the lattice structure and SOLIDWORKS for the perforated face sheet. The design variables of the bulk lattice are primarily dictated by the acoustic testing rig (in this case a normal incidence tube), since the active area of the liner needs to align with the active area of the test rig. The unit cell and face sheet design variables can be varied based on the desired performance of the liner and are the main drivers behind the acoustic performance of the specimen. The face sheet is designed to be a flat solid sheet with a user specified perforation pattern that aligns with the lattice underneath. Once the face sheet is designed in SOLIDWORKS, it is exported as a Parasolid and imported into nTop where it is attached to the top of the lattice to form a single implicit body. The single body is then exported as a .3MF mesh for manufacturing.

The liner core is printed on a Form 4 resin printer, which uses masked stereolithography (MSLA). The core is prepped in PreForm where it is carefully oriented with a 20° tilt about the Y-axis, supported, and sliced for printing. For acoustic purposes, the liner is required to be printed in a rigid material. The chosen resin also needs to be opaque, so that the features of the part are visible for image detection. To ensure proper resin evacuation after printing, the part is washed once upside down and once right-side up in a Form Wash station. With the excess resin removed, the part is cured in a Form Cure station. Support material is then removed from the part, making it ready for inspection.

3.2. Manual Measurement Method

While CT scanning may be considered the gold standard when it comes to analyzing complex lattice geometry for defects, there are instances, due to cost or resource restrictions, where it becomes impractical. Under these circumstances, it is important to have a systematic, alternative method for capturing stochastic manufacturing errors within printed parts. The first inspection method in this paper focuses on capturing stochastic variability through a combination of both manual measurements and 2D image inspection. One of the most limiting factors with this method is that, since a significant portion of the lattice in the liner core is enclosed by the outermost layer of Schwarz-P lattice cells and the face sheet, it is not possible to measure the internal lattice structure. Because of this, the assessment must be based on the critical assumption that measurements from the external lattice bulbs and face sheet are representative of the entire liner core. This assumption limits the accuracy of the measurement method, since there is no easy way to verify that the internal bulbs of the lattice share the same geometry as the outer surfaces. Future work is planned to verify that this assumption holds true.

There are several design variables that define the acoustic liner core and impact the acoustic performance. The overall length and width of the core are dictated by the testing apparatus and are not included as design variables for this paper since they are considered fixed. The face sheet is defined by a thickness, perforation diameter, and percent open area (POA). The lattice is defined by a unit cell size, wall thickness, and an isovalue. Measurements that can be taken manually using digital calipers (NEIKO 01407A) include the face sheet thickness, the unit cell size, and the wall thickness, as shown in Figure 2.

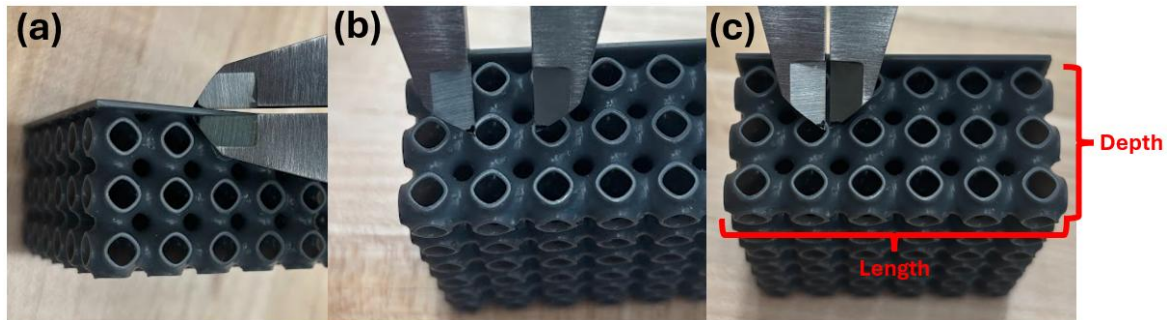


Figure 2. Measurement technique for the (a) face sheet thickness, (b) unit cell size, and (c) wall thickness.

The face sheet thickness is measured in several locations around the edge of the face sheet. The unit cell size is found by measuring the distance from the edge of a wall on one cell to the same edge on an adjacent cell. The wall thickness is found by measuring thickness of the walls at the pore openings. To account for the different print resolutions in the X-Y and Z directions on the Form 4 printer, the cell size and wall thickness measurements are grouped based on their orientation and location. Measurements taken on the sides (3x9 unit cell planes) along the length are considered “side length measurements” while measurements taken along the depth of the sides are considered “side depth measurements”. Additionally, measurements from the cells making up the 6x6 bottom of the core, defined as “bottom length measurements,” are kept separate due to the increased number of support structures attached to the bottom during printing. The removal process of such support material may cause bumps, chips, or cracks in the walls of the lattice, which can affect the quality of the measurements around the locations where support structures are attached.

Due to the 20° tilt used for manufacturing the sample, the X, Y, and Z axes of the printed core do not perfectly align with the axes of the printer; however, the X-Y and Z dimensions of the core should still be primarily impacted by the corresponding X-Y and Z resolutions of the printer.

In addition to variables that are measured manually, the perforation diameter, POA, and isovalue are also measured. Since these variables are too small to accurately measure with standard digital calipers, they are instead measured using a combination of several image processing tools. To accomplish this, it is necessary to first capture images of the sample from multiple views; this can be accomplished using a standard iPhone 15 back camera to photograph the face sheet, sides, and bottom of the liner core. The images are then imported into Adobe Lightroom where a lens correction is applied (Apple iPhone 15 back camera 5.96mm f/1.6) and the image is cropped to remove the excess background around the liner core. Additionally, perspective correction is applied to address any camera tilt and remove the remaining pin cushion distortion, bringing all the opposing edges parallel to each other. This process results in images of the core where the exposed sides match the physical part as much as possible.

After editing, the images can be used for inspection. To capture the perforation diameters and the POA, the face sheet image is imported into the analysis tool ImageJ [48]. The measurement scale is set, and the image is further cropped to only capture the area of the face sheet where the perforations are found. The image is then thresholded up to the point immediately before any of the perforations start to fade away. ImageJ's particle analysis tool is used to capture the individual areas of the face sheet perforations. Since the perforations in the face sheet are not perfectly circular, the effective diameter is estimated using their area. In some cases, excess resin or other contaminants can cause perforations to become partially blocked. Additionally, some residual noise particles in the image may be detected as very small areas. To remove the impact of the blockages and noise particles, any estimated diameter less than 80% of the nominal design diameter is removed from the data. This process yields a data set of as-printed estimated perforation diameters. To estimate the POA, the area of all the particles in the thresholded image are combined and divided by the total measured area of the face sheet.

The final value to measure is the isovalue. The main purpose of the isovalue is to control the volume ratio between the endo and exo void channels [7]. This means that the isovalue also controls the ratio of cross-sectional area between the two channels. Unfortunately, since the isovalue is a somewhat arbitrary constant when defining lattice geometry, measuring it can be difficult. For a Schwarz-P lattice, changing the isovalue changes the cross-sectional area ratio between the endo and exo pores as shown in Figure 3.

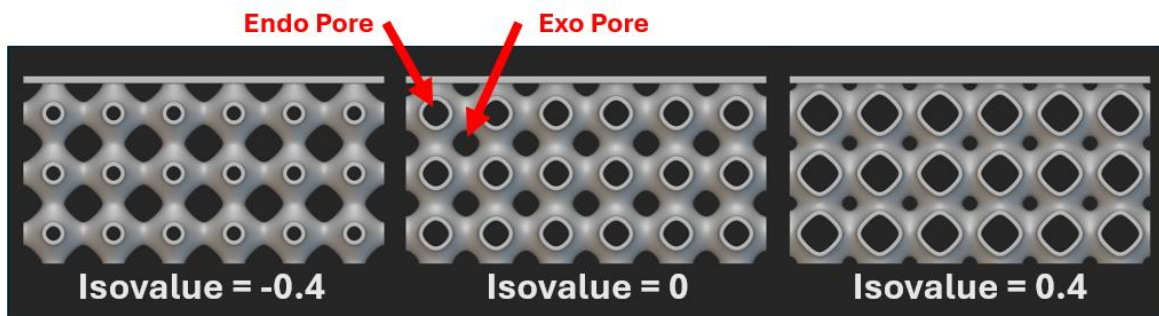


Figure 3. The effect of the isovalue on the cross-sectional area of the endo and exo lattice pores.

To find the ideal relationship between the isovalue and the cross-sectional area ratio of the pores, images of nTop models at different isovalues are carefully thresholded, cropped, and cleaned so that the area ratio of the pores, in pixels, can be used to establish a correlation with the isovalues. Figure 4 shows an example of a relationship found between isovalues and pore area ratios. With this relationship, the as-manufactured isovalue can be estimated by finding the ratios of the endo and exo pores in the printed core. First, the edited images of the core sides and bottom are run through a Canny edge detection algorithm [49]. Unwanted edges inside of pore areas are then removed and any small gaps in the pore edges are closed. Area ratios are then captured between each endo and corresponding exo pore. Finally, the as-manufactured isovalues are determined based off the isovalue/area ratio relationship established previously. It cannot be said for certain that the same relationship between isovalue and pore area ratio holds true beyond the external surface. All that can be said for sure is that the internal lattice structure aligns well with the external structure through visual inspection.

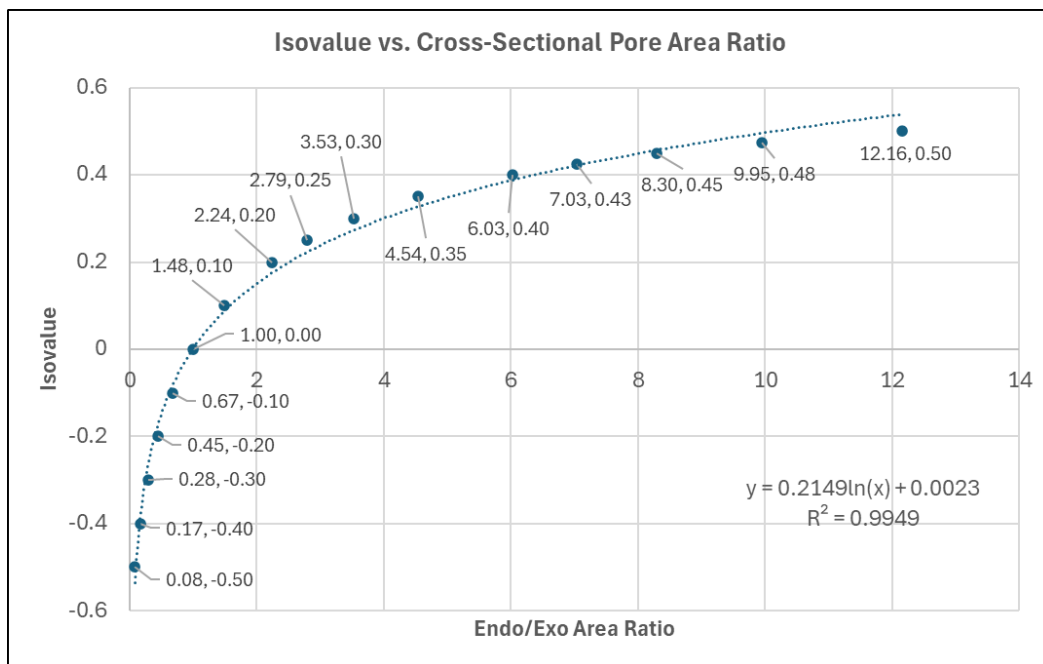


Figure 4. Relationship between the isovalue and the cross-sectional pore area ratio.

To capture the manufacturing deviation from the nominal design, each of the design variables is measured to find the average manufactured value and the standard deviation when possible. Crucially, several of these design variables can be measured in multiple locations to create distributions. A summary of each measured variable is provided in Table 1. While the proposed method intends to be systematic and as consistent as possible, some of the measurement techniques can still be somewhat subjective in nature. Due to uneven lighting, the user may be required to make a judgement call for what degree to threshold the face sheet perforation images. Face sheet perforation measurements could be verified using a second measure such as a pin gauge. The use of the calipers can also cause small variations in the measured data since increasing the clamping pressure can slightly compress the resin leading to smaller measured thickness values. The unit cell size measurements can also vary, as the user must properly align the calipers to the pore edges of the unit cell pores. Finally, the editing conducted on the image could lead to changes in the interpretation of the printed geometry, which could reflect in the final data.

Table 1. An overview of the variables measured for a Schwarz-P liner core.

| Measurement Tool | Variable | Measurement Technique |
|-------------------------------|----------------------|---|
| Digital calipers | Face Sheet Thickness | Measure the thickness around the edge of the face sheet. |
| | Unit Cell Size | Measure the offset unit cell size by finding the distance from the pore edge of one cell to the corresponding pore edge of an adjacent cell. |
| | Wall Thickness | Measure the wall thickness around the exposed lattice pore edges. |
| Image processing and analysis | Perforation Diameter | Threshold images of the face sheet so that only the perforations are visible and then batch measure the areas of the perforations. Use the areas to estimate the effective diameter of each perforation. |
| | Percent open area | Threshold images of the face sheet so that only the perforations are visible and then find the total area of the perforations. Divide the total perforation area by the total area of the face sheet. |
| | Isovalue | Use edge detection to capture clean edges of the endo and exo lattice pores. Find the cross-sectional area ratio between the corresponding endo and exo pores. Convert the ratios to isovalues using an isovalue vs. area ratio relationship calculated from the ideal model. |

3.3. Automated Screening Method

While Section 3.2 provides a systematic method to capturing manufacturing variations in printed specimens, manual measurements and physical inspection of prints bears costs in time and required effort. This can potentially limit the effectiveness of the method in screening for defects. As an alternative, computer vision solutions can alleviate these bottlenecks by leveraging machine learning and computer vision libraries to automate quality control and identification of defects and stochastic variation. Machine learning algorithms like neural networks can be trained to look for specific defects on printed parts. Libraries like OpenCV can find geometries in images, perform edge detection, and fit lines onto the images of printed parts. It is these techniques that form the backbone of the second of the two methods proposed in this paper.

As discussed previously, the defects on the outermost layer of Schwarz-P lattice cells and the face sheet can be split into two categories: structural defects and stochastic error. Structural defects, shown in Figure 5, are often in the form of chips and cracks in the lattice cells and blockages of face sheet perforations. On the face sheet, perforations can be partially or completely blocked by cured residual resin or contaminants from the wash process. These structural defects can stem from either the printing process itself or the post-processing procedure (e.g., support removal). While a framework for detecting these types of defects using neural networks has been established, the data sets of structural defects need to be expanded before machine learning can be implemented. The current training set for defect detection is 95 images with defects and 235 with no defects. This is from 2 individual prints. Runtimes on this set are fast, less than 5 mins for 10 epochs during model training, therefore scalability is likely high. For the purpose of this paper, any inspection for structural defects is done visually, with the assumption that additional failure data will soon enable the implementation of machine learning in the method. Image resolution defines the limit of defect identification. The size of structural defects that can be identified currently is around 3-6 mm. The second potential defect that must be evaluated is stochastic error. For the Schwarz-P lattice cells, there needs to be a consistency to the pore geometry. Ideally the pores are precisely the same geometry across the four sides and bottom containing the lattice. The face sheet also has four corners that need to be consistently square.

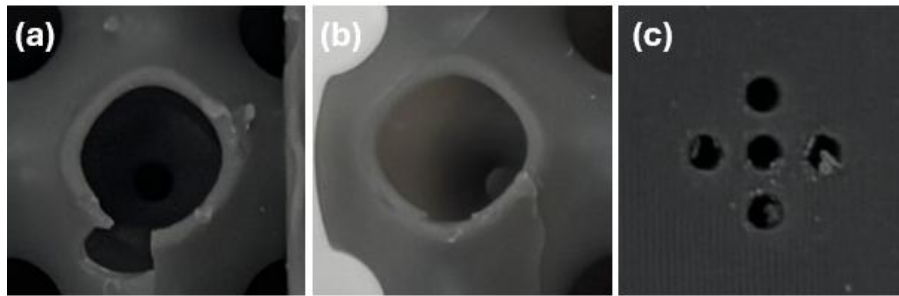


Figure 5. Structural defects in the form of (a) chips, (b) cracks, and (c) face sheet perforation blockages.

While both structural defects and stochastic error can be evaluated by the manual measurement technique discussed in Section 3.2, the automated screening method requires alternate means of capturing and measuring the liner geometry. The process starts by capturing images of the liner core using the same imaging procedure as the manual measurement method. Then, the unedited images of the 3D printed part are loaded into Altair AI Studio [50]. Within Altair AI Studio, a workflow is established that branches off to handle each image type separately. The bottom and sides of the Schwarz-P lattice go through the same process with the only difference being the size of the lattice; the bottom is a 6x6 unit cell arrangement, and the sides are each a 3x6 unit cell arrangement. This changes the location and number of pores in the image for the bottom and sides. To ensure image alignment, each side and bottom image is aligned using Scale-Invariant Feature Transform (SIFT) such that the centers of the pores are always at the same X and Y pixel location. Utilizing that position, each lattice pore is cropped from the original image, resized maintaining a 1-to-1 aspect ratio at 300 pixels, and converted to grayscale. Then, thresholding of the grayscale images looks for a specific hue of gray to filter on, where everything that matches that hue is set to 0 (black) and everything else is set to 255 (white) as shown in Figure 6. This approach was advantageous because the depth of the pores created a darker region inside the pore.

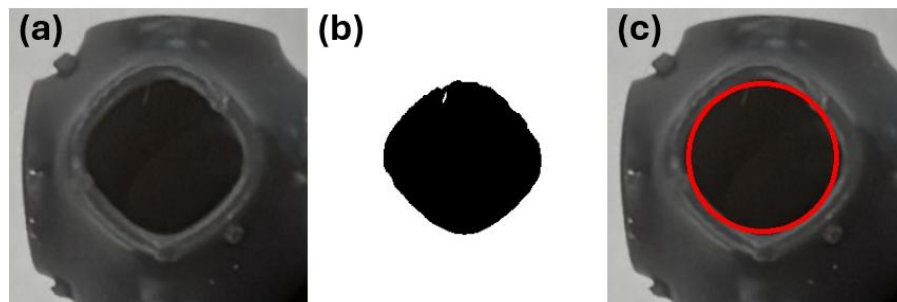


Figure 6. Unit cell after (a) crop and resize, (b) thresholding, and (c) an ellipse is fit to the pore.

To calculate the symmetry of each pore, OpenCV's fit ellipse function is applied to the pore images resulting in an output that delivers major and minor axis lengths in pixels along with the X and Y pixel coordinates for its center. While it is known that the pores are not ellipses, the difference in the major and minor axis can be used to determine the symmetric consistency of the pores.

The next component of the workflow is responsible for measuring all four corner angles of the face sheet. As shown in Figure 7, OpenCV's Canny edge detection and HoughLinesP functions are applied to the image to fit lines to the edges of the face sheet. The results are a series of line coordinates in the form of (X_1, Y_1) and (X_2, Y_2) . In order to find which lines are aligned with the face sheet corner, the distance between X_1 and Y_1 and the top left and bottom left of the image is calculated. The distance between X_2 and Y_2 and the top right and bottom right of the image is also calculated, with the two minimum distances then paired as a corner. The angle between corner lines is calculated in Python by using the slopes of the two lines.

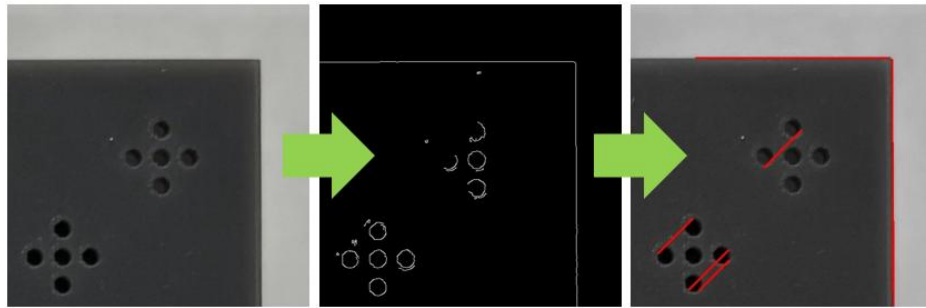


Figure 7. Line fitting process for the face sheet corners.

Once the computer vision calculations are done, the results are then used to determine a “pass” or “fail” for that inspection. In a single specimen, there are 633 inspections made, comprised of 108 pores checked for symmetry, chips, and cracks, 4 corner angles of the face sheet, and 305 perforations checked for blockages. Starting with the unit cells, pores visually identified to contain a chip or crack receive a failure in their corresponding category. Pore symmetry is found using the difference between the major and minor axis of the fit ellipse; a value of 0 suggests a symmetric circle while a value tending to infinity suggests a straight line. This difference helps assess how uniform the pores are across the print. It is known that the images contain some lens distortion, but due to an inconsistent imaging process, this distortion cannot be confidently corrected. Instead, lens distortion is accounted for by imposing different failure margins for the axis difference, with a larger failure margin for pores on the edges of the print compared to pores at the center of the image. Failure for the symmetry of the pore is measured in pixels for each lattice position, with the outermost position, lattice columns 1 or 6, set to a difference of 10 or more pixels, columns 2 or 5 set to a difference of 9 or more pixels, and columns 3 or 4, set to a difference of 8 or more pixels. Any pore whose axis difference is outside of these ranges is considered to “fail” for that inspection. A proper camera rig would keep the images consistent, allowing for confident correction of distortion and removal of the difference in pass/fail margins. For the face sheet, any perforations visually inspected to contain a significant blockage result in a failure for that inspection. Any angles that are less than 88.5 degrees result in a failure for that inspection. The final result is output as the total number of failures from the total number of inspections.

4. Two Case Studies for Method Demonstration

Both methods offer unique information about the manufacturing quality of the liner cores, as defined by Figure 1, with the manual measurement method giving insight into the dimensional accuracy and distributions and the automated screening method evaluating the parts for print defects and geometric consistency. To demonstrate the two methods of detecting stochastic

manufacturing error and defects, each method was applied to the same liner core design. Although the methods have been developed in a way that can be adapted to measure other types of TPMS lattices, this paper focuses on a core that uses a Schwarz-P lattice. This section will describe the specific design of the core that was analyzed (4.1.), the execution of the manual measurement method (4.2.), and the execution of the automated screening method (4.3.).

4.1. Test Liner Core Design

The first step in demonstrating the two defect detection methods was to develop a representative acoustic liner core. As discussed, the overall length and width of the core are dictated by the normal incidence tube testing apparatus. The core used for these case studies was designed with both a length and width of 50.8 mm. While these dimensions are not a focus of our error identification, they will be important for measuring the manufactured POA of the sample. The variables used to design the face sheet included a face sheet thickness of 1 mm, perforation diameter of 0.8 mm, and a POA of 5.94% that was dictated by the perforation pattern of the face sheet. The TPMS Schwarz-P lattice was designed with a uniform wall thickness of 0.6 mm, unit cell size of approximately 8.47 mm, and an isovalue of 0.2. The final printed core is shown with and without supports in Figure 8. The core was printed in Form Tough 2000 resin at a layer height of 0.05 mm and a 20° tilt. It was then washed in the Form Wash upside-down for 10 minutes and right-side up for 10 minutes. Finally, it was cured in the Form Cure at 70°C for 60 minutes.

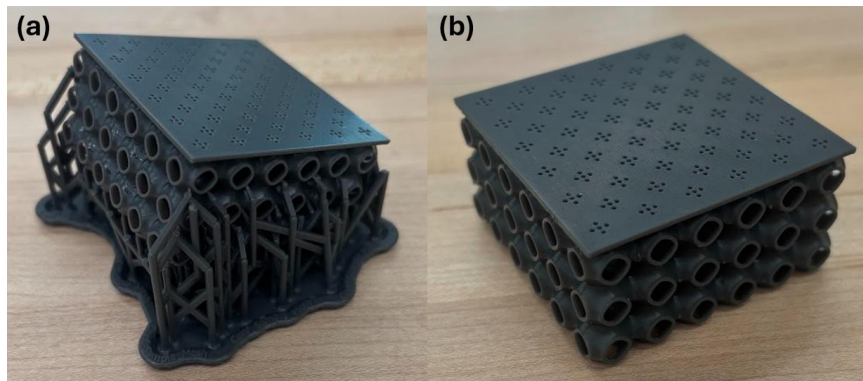


Figure 8. The printed liner core (a) with supports and (b) without supports.

4.2. Manual Measurement Method Execution

Using the representative liner core, the manual measurement method from Section 3.2 was performed. This starts by gathering measurements through the use of calipers. The face sheet thickness was measured 12 times per side, for a total of 48 measurements. On each side, six measurements were aligned with the endo pores of the lattice and the remaining six measurements were aligned with the exo pores. During this process, it was found that the face sheet thickness where the lattice connected to the face sheet was slightly thicker than the thickness aligned with the exo pores. This was most likely due to small amounts of excess resin that gathered around the connection points leading to small fillets instead of sharp edges. The unit cell size was measured in the side length, side depth, and bottom length orientations, as shown in Figure 9. Based on the geometry of the lattice, a total of 60 measurements were captured for the side length orientation, 48 for the side depth orientation, and 60 for the bottom length orientation. The last measured variable was the wall thickness of the lattice. Figure 9 also shows how these measurements were collected similar to the cell size, with 144 measurements captured for each of the three orientations.

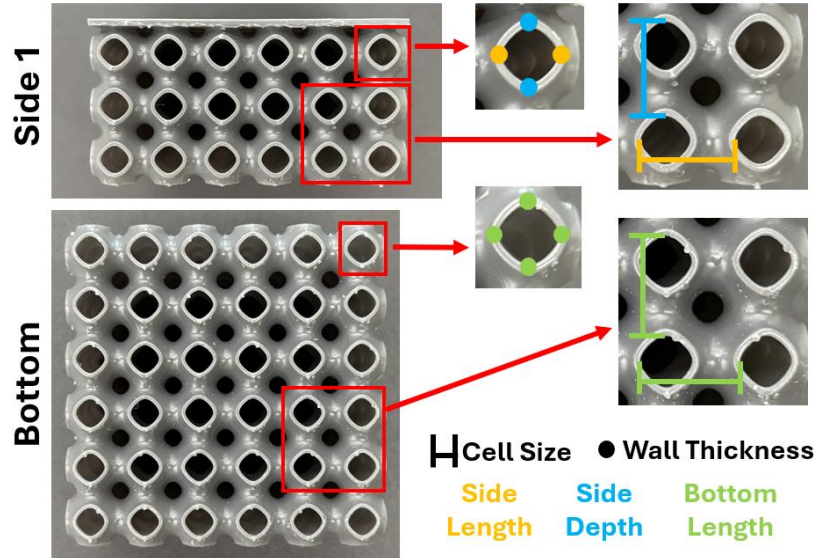


Figure 9. Measurement locations and directions for each cell size and wall thickness orientation.

Once the face sheet thickness, cell size, and wall thickness had been measured with calipers, the rest of the measurements were found using image processing tools, starting with perforation diameters. Figure 10 shows a comparison between the original images opened in ImageJ and the thresholded image used for the area estimations on the perforations. Using the thresholded image, particle analysis yielded 459 area measurements. The effective diameters of the particles were found by converting the areas to diameters using simple circle geometry. In some perforations, small flakes can be seen partially blocking the openings. This was suspected to be small contaminants from the shared Form Wash, which got stuck during the wash process. The flakes caused some of the perforations to appear partially blocked or split into multiple sections in the thresholded image. After removing the diameters of both noise particles and significantly blocked/split perforations, the data was reduced to 297 effective diameters. With the original perforation count being 305, this means that only 8 perforations were considered significantly blocked and the rest of the area measurements were captured due to small noise particles. The particle analysis also outputs a total area, which was used as the total open area of the face sheet. The as-printed cross-sectional area of the face sheet was found by measuring the length and width of the face sheet, which was 51.3 mm and 50.03 mm, respectively. By dividing the open area by the as-printed cross-sectional area of the face sheet the manufactured POA was found.

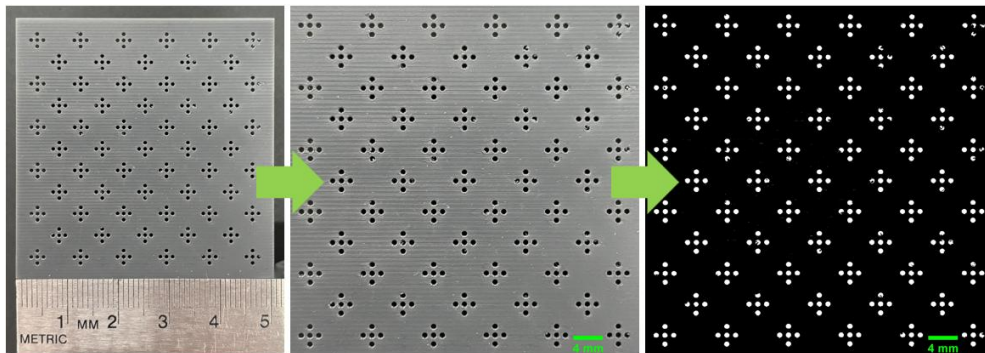


Figure 10. Face sheet image preparation for perforation area measurements.

The final design variable measured was the isovalue. Images of the sides and bottom of the sample were run through the Canny edge detection software and cleaned in ImageJ so that a section of the endo and exo pore areas could be measured in terms of pixels, as shown in Figure 11. The endo pore area was then divided by the exo pore area to find the ratio between the two and could then be related to an isovalue. Through a similar measurement technique of the ideal nTop model at several different isovalues, the relationship from Figure 4 was found between the endo/exo pore area ratio and the isovalue. This relationship was then used to convert the manufactured pore ratios into isovalues. By analyzing each of the sides and the bottom of the sample, a total of 65 pore area ratios, and thus isovalues, were measured.

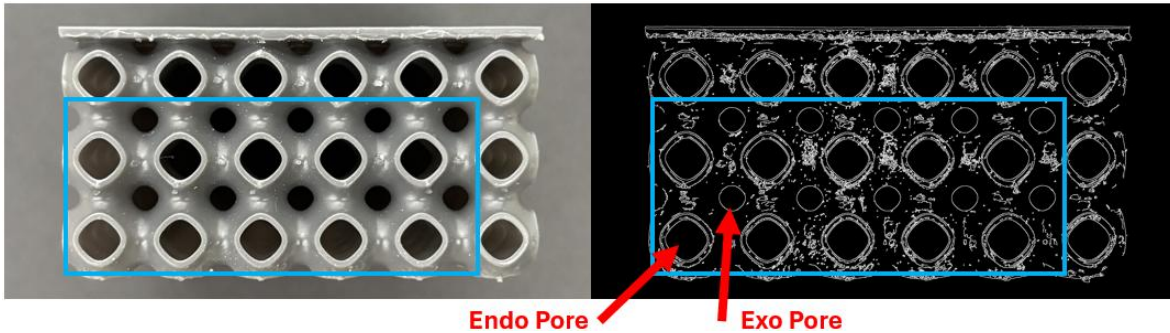


Figure 11. Conversion of lattice to binary edges for the purpose of measuring the areas of the endo and exo pores outlined in blue.

All of the collected data was used to find the average, standard deviation, minimum, and maximum values for each design variable, as shown in Table 2. As can be seen, every design variable, except perforation diameter and POA, was found to be slightly oversized on average. This shows that most of the design variables would need to be undersized before printing in order to achieve the correct nominal dimensions in the manufactured part. Conversely, the perforation diameter and POA would need to be slightly oversized before printing. In the event that visual inspection of the distributions of the data is needed, the collected raw data can also be used to create histograms for several design variables.

Table 2. Summary of design variable measurements.

| Variable | Nominal | Average | Standard deviation | Minimum | Maximum |
|--------------------------------|---------|---------|--------------------|---------|---------|
| Face Sheet Thickness | 1 mm | 1.17 mm | 0.05 mm | 1.09 mm | 1.29 mm |
| Unit Cell Size (Side Length) | 8.47 mm | 8.51 mm | 0.04 mm | 8.43 mm | 8.61 mm |
| Unit Cell Size (Side Depth) | 8.47 mm | 8.51 mm | 0.05 mm | 8.42 mm | 8.59 mm |
| Unit Cell Size (Bottom Length) | 8.47 mm | 8.50 mm | 0.04 mm | 8.42 mm | 8.59 mm |
| Wall Thickness (Side Length) | 0.6 mm | 0.64 mm | 0.03 mm | 0.55 mm | 0.71 mm |
| Wall Thickness (Side Depth) | 0.6 mm | 0.73 mm | 0.05 mm | 0.64 mm | 0.87 mm |
| Wall Thickness (Bottom Length) | 0.6 mm | 0.63 mm | 0.04 mm | 0.55 mm | 0.72 mm |
| Perforation Diameter | 0.8 mm | 0.69 mm | 0.02 mm | 0.64 mm | 0.72 mm |
| Percent Open Area (POA) | 5.94% | 4.26% | N/A | N/A | N/A |
| Isovalue | 0.2 | 0.201 | 0.003 | 0.192 | 0.207 |

4.3. Automated Defect Screening Method Execution

While the manual measurement method was able to output information regarding dimensional and geometric accuracy, this section demonstrates the ability of the automated screening method to detect significant defects and stochastic errors in the print consistency. First, images of the representative core were taken and analyzed with the automated screening method. The AI Studio workflow received six representative images (the bottom, sides 1-4, and the face sheet) and processed them individually. The first result was the pore uniformity and defect detection for the bottom of the Schwarz-P lattice. Note that, to identify the location of a pore within the lattice array, we will use the nomenclature of “Pore (row, column).” Automated inspection of the bottom discovered irregularity in Pore (2, 5) and visual inspection discovered no chips or cracks for an output of 1 flagged defect out of 108 inspections. The first side of the Schwarz-P lattice, which switches to the 3x6 lattice array, contained no defects, resulting in a count of 0 defects out of 54 inspections. The second side contained irregularities at Pore (3, 4) and (3, 5) with no chips or cracks for an output of 2 defects out of 54 inspections. The third side contained an irregularity at Pore (3, 3) and no other visual defects for an output of 1 out of 54. The fourth side contained the highest uniformity deviation with 7 failures for an output of 7 out of 54. Figure 12 shows the uniformity plots for the bottom and fourth side of the liner core. This plot depicts if the differences in major and minor axes of the pores on the bottom or sides of the lattice exceeded the failure threshold. Larger circles indicate larger differences between the axes, and red circles indicate that the difference between the axes surpassed the failure value for the corresponding pore location.

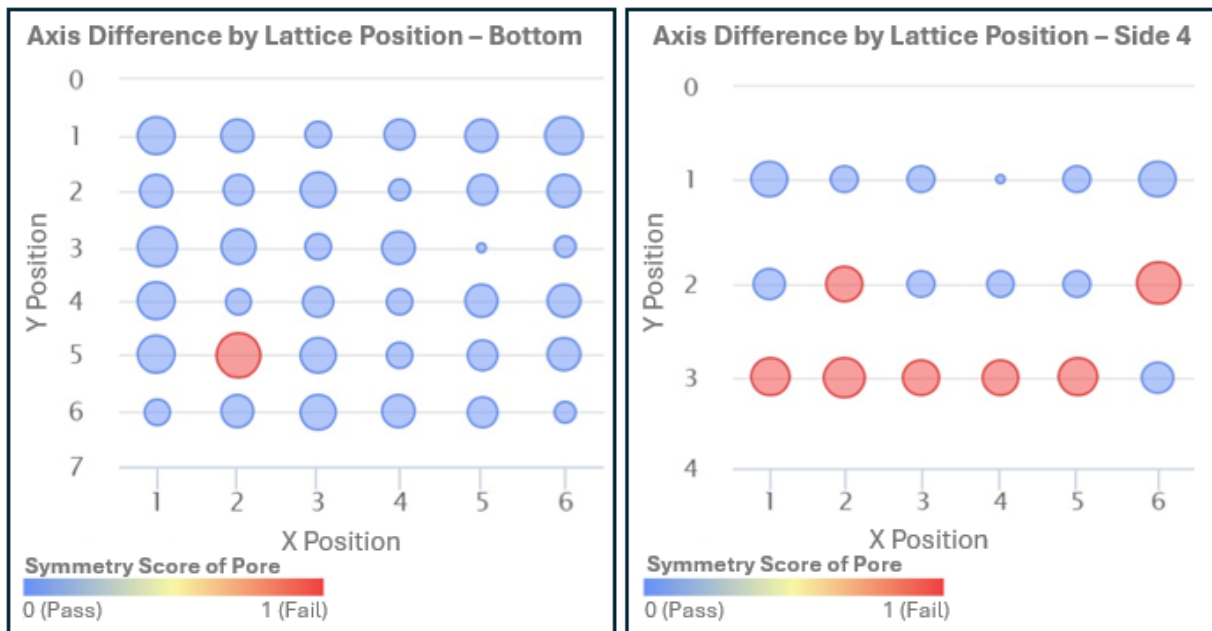


Figure 12. Axes difference in pores on the bottom of the print (left) and the fourth side (right).

The final inspection was the face sheet. After applying the edge detection and fitting the Hough lines to the face sheet image, all angles were above the 88.5 threshold. The visual inspection of the perforations revealed 15 partial blockages for a score of 15 failures out of 309 inspections. The print, when checked for all defects, contained 26 failures out of 633 inspections for a 4.1% defect rate. Broken down into stochastic error, 11 of 108 pores had inconsistently shaped openings and the face sheet's angles were square. Structural defects were only in the form of perforation

blockages, which could be punched out to the correct size and shape for testing purposes if necessary. While most of this data does not provide dimensional information of the printed core, it can be used to quickly judge the quality of a print and determine which prints are acceptable for testing. For example, since this core only contained a 4.1% defect rate, it would likely be a viable sample for testing. Cores printed with higher defect rates could be quickly identified and reprinted before testing.

5. Conclusions and Future Work

Two methods are presented for capturing manufactured errors and defects in printed TPMS lattice structures that show promise as acoustic liners for aircraft engines. The first uses manual measurements taken from the specimen and image analysis tools to compile data sets of the produced stochastic error of design variables in the printed parts. The second method automatically processes images of the printed liner specimen along with user input from visual inspection to assess the print quality. A case study was conducted to demonstrate the possible results obtained from each method. The results highlight how these two methods are capable of identifying significant defects and stochastic error in the geometry of a test design for an acoustic liner core.

Future work is needed to increase the applicability and accuracy of each method. For the manual measurement method, verification processes should be used to assess the accuracy of the measurements. While this work is meant to establish an alternative to CT scan inspection, a CT scan of the part could be used as the ground truth to verify the new measurement methods. Additionally, while the method used to measure the isovalue in this paper is functionally viable, the image processing is time intensive and other methods could be investigated. While these tasks could improve the accuracy of the measurements, the main goal is to incorporate the findings of the stochastic error analysis into acoustic simulation studies in an effort to improve the predictability of printed liners. For the automated screening method, future work will incorporate the crack/chip and face sheet perforation blockage detection into the screening algorithm using image detection and neural networks. This will remove the visual inspection step in the process, but depends on the intake of a large data set not yet available. Work should also be done to determine the significance (in this work, the acoustic performance) of each defect, so that they can be properly weighed when determining an overall final evaluation of manufactured liner quality. Rigorous validation through the use of purposefully produced defect-ridden samples will help to stress test the automated screening method. Expanding the sample size of the case studies for both methods by measuring multiple liner cores will increase the confidence in the consistency of each approach. Finally, the combination of the two methods could yield a comprehensive data set used to assess the print quality of acoustic liners in both a lab and an industry setting.

6. Acknowledgements

This research was funded through the U.S. Federal Aviation Administration Office of Environment and Energy through ASCENT, the FAA Center of Excellence for Alternative Jet Fuels and the Environment, Project 79 through FAA Award Number 13-C-AJFE-PSU-113 under the supervision of Pierre Mulgrave. Any opinions, findings, conclusions or recommendations expressed in this material are those of the authors and do not necessarily reflect the views of the FAA.

7. References

- [1] Konopka, W., Pawlaczyk-Luszczynska, M., and Śliwińska-Kowalska, M., 2014, “The Influence of Jet Engine Noise on Hearing of Technical Staff,” *Med Pr*, **65**(5), pp. 583–592.
- [2] Yan, Q., Xue, D., Mu, Q., Yang, J., Gao, X., and Huang, W., 2023, “Acoustic Experimental Technology for Aircraft Nacelle Liner,” *Aerospace*, **10**(1), p. 56. <https://doi.org/10.3390/aerospace10010056>.
- [3] Winkler, J., Mendoza, J. M., Reimann, C. A., Homma, K., and Alonso, J. S., 2021, “High Fidelity Modeling Tools for Engine Liner Design and Screening of Advanced Concepts,” *International Journal of Aeroacoustics*, **20**(5–7), pp. 530–560. <https://doi.org/10.1177/1475472X211023884>.
- [4] Neubauer, M., Genßler, J., Radmann, V., Kohlenberg, F., Pohl, M., Böhme, K., Knobloch, K., Sarradj, E., Höschler, K., Modler, N., and Enghardt, L., 2023, “Experimental and Numerical Investigation of Novel Acoustic Liners and Their Design for Aero-Engine Applications,” *Aerospace*, **10**(1), p. 5. <https://doi.org/10.3390/aerospace10010005>.
- [5] Sutliff, D. L., Nark, D. M., and Jones, M. G., 2021, “Multi-Degree-of-Freedom Liner Development: Concept to Flight Test,” *International Journal of Aeroacoustics*, **20**(5–7), pp. 792–825. <https://doi.org/10.1177/1475472X211023860>.
- [6] Jonnala, U. K., K. L. R., and Y, R. K., 2024, “Design and Development of Novel Lattice Structures for Optimum Energy Absorption,” *Journal of Engineering Materials and Technology*, **146**(3), p. 031010. <https://doi.org/10.1115/1.4064752>.
- [7] Kumar, R., Ramkumar, J., and Balani, K., 2024, “Design and Parametrization of TPMS Lattice Using Computational and Experimental Approach,” *Eng. Res. Express*, **6**(3), p. 035556. <https://doi.org/10.1088/2631-8695/ad7109>.
- [8] Novak, N., Al-Ketan, O., Borovinšek, M., Krstulović-Opara, L., Rowshan, R., Vesenjak, M., and Ren, Z., 2021, “Development of Novel Hybrid TPMS Cellular Lattices and Their Mechanical Characterisation,” *Journal of Materials Research and Technology*, **15**, pp. 1318–1329. <https://doi.org/10.1016/j.jmrt.2021.08.092>.
- [9] Modrek, M., Viswanath, A., Khan, K. A., Ali, M. I. H., and Abu Al-Rub, R. K., 2022, “An Optimization Case Study to Design Additively Manufacturable Porous Heat Sinks Based on Triply Periodic Minimal Surface (TPMS) Lattices,” *Case Studies in Thermal Engineering*, **36**, p. 102161. <https://doi.org/10.1016/j.csite.2022.102161>.
- [10] Chouhan, G., Bidare, P., and Bala Murali, G., 2024, “Triply Periodic Minimal Surface Based Lattices for Acoustic Performance,” *Noise & Vibration Worldwide*, **55**(8), pp. 454–468. <https://doi.org/10.1177/09574565241270201>.
- [11] Jin, M., Feng, Q., Fan, X., Luo, Z., Tang, Q., Song, J., Ma, S., Nie, Y., Jin, P., and Zhao, M., 2022, “Investigation on the Mechanical Properties of TPMS Porous Structures Fabricated by Laser Powder Bed Fusion,” *Journal of Manufacturing Processes*, **76**, pp. 559–574. <https://doi.org/10.1016/j.jmapro.2022.02.035>.
- [12] Jones, A., Leary, M., Bateman, S., and Easton, M., 2022, “Parametric Design and Evaluation of TPMS-like Cellular Solids,” *Materials & Design*, **221**, p. 110908. <https://doi.org/10.1016/j.matdes.2022.110908>.
- [13] Li, X., Yu, X., and Zhai, W., 2021, “Additively Manufactured Deformation-Recoverable and Broadband Sound-Absorbing Microlattice Inspired by the Concept of Traditional Perforated Panels,” *Advanced Materials*, **33**(44), p. 2104552. <https://doi.org/10.1002/adma.202104552>.

- [14] Carneiro, V. H., Rawson, S. D., Puga, H., and Withers, P. J., 2021, “Macro-, Meso- and Microstructural Characterization of Metallic Lattice Structures Manufactured by Additive Manufacturing Assisted Investment Casting,” *Sci Rep*, **11**(1), p. 4974. <https://doi.org/10.1038/s41598-021-84524-y>.
- [15] Alghamdi, A., Maconachie, T., Downing, D., Brandt, M., Qian, M., and Leary, M., 2020, “Effect of Additive Manufactured Lattice Defects on Mechanical Properties: An Automated Method for the Enhancement of Lattice Geometry,” *Int J Adv Manuf Technol*, **108**(3), pp. 957–971. <https://doi.org/10.1007/s00170-020-05394-8>.
- [16] Paxton, N. C., Zhao, J., and Sauret, E., 2024, “Polymer 3D Printing in Perspective: Assessing Challenges and Opportunities in Industrial Translation against the Metal Benchmark,” *Int J Adv Manuf Technol*, **133**(1), pp. 59–80. <https://doi.org/10.1007/s00170-024-13744-z>.
- [17] Chouhan, G., Bidare, P., Doodi, R., and Murali, G. B., 2023, “Identification of Surface Defects on an SLA-Printed Gyroid Lattice Structure,” *Design in the Era of Industry 4.0, Volume 2*, A. Chakrabarti, and V. Singh, eds., Springer Nature Singapore, Singapore, pp. 697–707. https://doi.org/10.1007/978-981-99-0264-4_58.
- [18] Salem, H., Carter, L. N., Attallah, M. M., and Salem, H. G., 2019, “Influence of Processing Parameters on Internal Porosity and Types of Defects Formed in Ti6Al4V Lattice Structure Fabricated by Selective Laser Melting,” *Materials Science and Engineering: A*, **767**, p. 138387. <https://doi.org/10.1016/j.msea.2019.138387>.
- [19] Ning, J., Sievers, D. E., Garmestani, H., and Liang, S. Y., 2020, “Analytical Modeling of Part Porosity in Metal Additive Manufacturing,” *International Journal of Mechanical Sciences*, **172**, p. 105428. <https://doi.org/10.1016/j.ijmecsci.2020.105428>.
- [20] Liu, Y. J., Li, S. J., Wang, H. L., Hou, W. T., Hao, Y. L., Yang, R., Sercombe, T. B., and Zhang, L. C., 2016, “Microstructure, Defects and Mechanical Behavior of Beta-Type Titanium Porous Structures Manufactured by Electron Beam Melting and Selective Laser Melting,” *Acta Materialia*, **113**, pp. 56–67. <https://doi.org/10.1016/j.actamat.2016.04.029>.
- [21] Chen, L.-Y., Liang, S.-X., Liu, Y., and Zhang, L.-C., 2021, “Additive Manufacturing of Metallic Lattice Structures: Unconstrained Design, Accurate Fabrication, Fascinated Performances, and Challenges,” *Materials Science and Engineering: R: Reports*, **146**, p. 100648. <https://doi.org/10.1016/j.mser.2021.100648>.
- [22] Ciochon, A., Kennedy, J., Leiba, R., Flanagan, L., and Culleton, M., 2023, “The Impact of Surface Roughness on an Additively Manufactured Acoustic Material: An Experimental and Numerical Investigation,” *Journal of Sound and Vibration*, **546**, p. 117434. <https://doi.org/10.1016/j.jsv.2022.117434>.
- [23] Kennedy, J., Flanagan, L., Dowling, L., Bennett, G. J., Rice, H., and Trimble, D., 2019, “The Influence of Additive Manufacturing Processes on the Performance of a Periodic Acoustic Metamaterial,” *International Journal of Polymer Science*, **2019**(1), p. 7029143. <https://doi.org/10.1155/2019/7029143>.
- [24] Li, D., Qin, R., Chen, B., and Zhou, J., 2021, “Analysis of Mechanical Properties of Lattice Structures with Stochastic Geometric Defects in Additive Manufacturing,” *Materials Science and Engineering: A*, **822**, p. 141666. <https://doi.org/10.1016/j.msea.2021.141666>.
- [25] Van Bael, S., Kerckhofs, G., Moesen, M., Pyka, G., Schrooten, J., and Kruth, J. P., 2011, “Micro-CT-Based Improvement of Geometrical and Mechanical Controllability of

- Selective Laser Melted Ti6Al4V Porous Structures,” *Materials Science and Engineering: A*, **528**(24), pp. 7423–7431. <https://doi.org/10.1016/j.msea.2011.06.045>.
- [26] Hassan, I. M., Enab, T. A., Fouda, N., and Eldesouky, I., 2023, “Design, Fabrication, and Evaluation of Functionally Graded Triply Periodic Minimal Surface Structures Fabricated by 3D Printing,” *J Braz. Soc. Mech. Sci. Eng.*, **45**(1), p. 66. <https://doi.org/10.1007/s40430-022-03972-3>.
- [27] Yang, L., Ferrucci, M., Mertens, R., Dewulf, W., Yan, C., Shi, Y., and Yang, S., 2020, “An Investigation into the Effect of Gradients on the Manufacturing Fidelity of Triply Periodic Minimal Surface Structures with Graded Density Fabricated by Selective Laser Melting,” *Journal of Materials Processing Technology*, **275**, p. 116367. <https://doi.org/10.1016/j.jmatprotec.2019.116367>.
- [28] Zhang, L., Lifton, J., Hu, Z., Hong, R., and Feih, S., 2022, “Influence of Geometric Defects on the Compression Behaviour of Thin Shell Lattices Fabricated by Micro Laser Powder Bed Fusion,” *Additive Manufacturing*, **58**, p. 103038. <https://doi.org/10.1016/j.addma.2022.103038>.
- [29] Nowacki, B., Kowol, P., Koziol, M., Olesik, P., Wiczorek, J., and Waclawiak, K., 2021, “Effect of Post-Process Curing and Washing Time on Mechanical Properties of mSLA Printouts,” *Materials*, **14**(17), p. 4856. <https://doi.org/10.3390/ma14174856>.
- [30] Peloquin, J., Han, Y., and Gall, K., 2023, “Printability and Mechanical Behavior as a Function of Base Material, Structure, and a Wide Range of Porosities for Polymer Lattice Structures Fabricated by Vat-Based 3D Printing,” *Additive Manufacturing*, **78**, p. 103892. <https://doi.org/10.1016/j.addma.2023.103892>.
- [31] Long, C., Jiang, L., Xiong, S., Liu, Z., Liu, C., and Chen, Z., 2024, “Effective Post-Cleaning Strategy for Vat Photopolymerization 3D Printed Complex-Structured Polymer-Derived Ceramics,” *Additive Manufacturing*, **94**, p. 104456. <https://doi.org/10.1016/j.addma.2024.104456>.
- [32] Karalekas, D., Rapti, D., Gdoutos, E. E., and Aggelopoulos, A., 2002, “Investigation of Shrinkage-Induced Stresses in Stereolithography Photo-Curable Resins,” *Experimental Mechanics*, **42**(4), pp. 439–444. <https://doi.org/10.1007/BF02412150>.
- [33] Tang, T., Nawab, P. K., Prabhudesai, P., Alfarhan, S., Pesqueira, I., VanWormer, K., Li, J., Li, D., Jin, K., and Li, X., 2025, “Sustainable Vat Photopolymerization of Complex Functional Structures with Fast Dissolvable and Recyclable Supports,” *Virtual and Physical Prototyping*, **20**(1), p. 2499452. <https://doi.org/10.1080/17452759.2025.2499452>.
- [34] De Chiffre, L., Carmignato, S., Kruth, J.-P., Schmitt, R., and Weckenmann, A., 2014, “Industrial Applications of Computed Tomography,” *CIRP Annals*, **63**(2), pp. 655–677. <https://doi.org/10.1016/j.cirp.2014.05.011>.
- [35] du Plessis, A., Yadroitsev, I., Yadroitsava, I., and Le Roux, S. G., 2018, “X-Ray Microcomputed Tomography in Additive Manufacturing: A Review of the Current Technology and Applications,” *3D Printing and Additive Manufacturing*, **5**(3), pp. 227–247. <https://doi.org/10.1089/3dp.2018.0060>.
- [36] Khosravani, M. R., and Reinicke, T., 2020, “On the Use of X-Ray Computed Tomography in Assessment of 3D-Printed Components,” *J Nondestruct Eval*, **39**(4), p. 75. <https://doi.org/10.1007/s10921-020-00721-1>.
- [37] Ziabari, A., Venkatakrisnan, S. V., Snow, Z., Lisovich, A., Sprayberry, M., Brackman, P., Frederick, C., Bhattad, P., Graham, S., Bingham, P., Dehoff, R., Plotkowski, A., and Paquit, V., 2023, “Enabling Rapid X-Ray CT Characterisation for Additive Manufacturing

- Using CAD Models and Deep Learning-Based Reconstruction,” *npj Comput Mater*, **9**(1), pp. 1–10. <https://doi.org/10.1038/s41524-023-01032-5>.
- [38] Thompson, A., Maskery, I., and Leach, R. K., 2016, “X-Ray Computed Tomography for Additive Manufacturing: A Review,” *Meas. Sci. Technol.*, **27**(7), p. 072001. <https://doi.org/10.1088/0957-0233/27/7/072001>.
- [39] Mohammed, A., and Abdullah, A., 2018, “SCANNING ELECTRON MICROSCOPY (SEM): A REVIEW,” *Proceedings of 2018 International Conference on Hydraulics and Pneumatics - HERVEX*, Băile Govora, Romania, pp. 77–85. [Online]. Available: <https://fluidas.ro/hervex/proceedings2018/77-85.pdf>.
- [40] Cansizoglu, O., Harrysson, O., Cormier, D., West, H., and Mahale, T., 2008, “Properties of Ti–6Al–4V Non-Stochastic Lattice Structures Fabricated via Electron Beam Melting,” *Materials Science and Engineering: A*, **492**(1–2), pp. 468–474. <https://doi.org/10.1016/j.msea.2008.04.002>.
- [41] Gabrieli, R., Wenger, R., Mazza, M., Verné, E., and Baino, F., 2024, “Design, Stereolithographic 3D Printing, and Characterization of TPMS Scaffolds,” *Materials*, **17**(3), p. 654. <https://doi.org/10.3390/ma17030654>.
- [42] Hussain, S., Alagha, A. N., Haidemenopoulos, G. N., and Zaki, W., 2023, “Microstructural and Surface Analysis of NiTi TPMS Lattice Sections Fabricated by Laser Powder Bed Fusion,” *Journal of Manufacturing Processes*, **102**, pp. 375–386. <https://doi.org/10.1016/j.jmapro.2023.07.055>.
- [43] Al-Meslemi, Y., Ferreira, K., Mehdi-Souzani, C., Obaton, A.-F., Nouira, H., and Anwer, N., 2023, “Quality Control for Additive Manufacturing,” *Springer Handbook of Additive Manufacturing*, E. Pei, A. Bernard, D. Gu, C. Klahn, M. Monzón, M. Petersen, and T. Sun, eds., Springer International Publishing, Cham, pp. 797–819. https://doi.org/10.1007/978-3-031-20752-5_47.
- [44] Wilbig, J., Borges De Oliveira, F., Obaton, A.-F., Schwentenwein, M., Rübner, K., and Günster, J., 2020, “Defect Detection in Additively Manufactured Lattices,” *Open Ceramics*, **3**, p. 100020. <https://doi.org/10.1016/j.oceram.2020.100020>.
- [45] Obaton, A.-F., Wang, Y., Butsch, B., and Huang, Q., 2021, “A Non-Destructive Resonant Acoustic Testing and Defect Classification of Additively Manufactured Lattice Structures,” *Weld World*, **65**(3), pp. 361–371. <https://doi.org/10.1007/s40194-020-01034-7>.
- [46] Zhang, Z., Zhang, Y., Wen, Y., Fu, K., and Luo, X., 2022, “Intelligent Defect Detection Method for Additive Manufactured Lattice Structures Based on a Modified YOLOv3 Model,” *J Nondestruct Eval*, **41**(1), p. 3. <https://doi.org/10.1007/s10921-021-00835-0>.
- [47] Ma, X., and Su, Z., 2020, “Development of Acoustic Liner in Aero Engine: A Review,” *Sci. China Technol. Sci.*, **63**(12), pp. 2491–2504. <https://doi.org/10.1007/s11431-019-1501-3>.
- [48] Rasband, W., 1997, “ImageJ.” [Online]. Available: <https://imagej.net/ij/>.
- [49] Canny, J., 1986, “A Computational Approach to Edge Detection,” *IEEE Transactions on Pattern Analysis and Machine Intelligence*, **PAMI-8**(6), pp. 679–698. <https://doi.org/10.1109/TPAMI.1986.4767851>.
- [50] Altair Engineering, Inc., 2024, “Altair AI Studio.” [Online]. Available: <https://altair.com/altair-ai-studio>.